PCCP

ROYAL SOCIETY OF CHEMISTRY

PAPER

View Article Online
View Journal | View Issue

Cite this: *Phys. Chem. Chem. Phys.*, 2024, **26**, 8641

Color tunable luminescence in ThO_2:Er^{3+},Yb^{3+} nanocrystals: a promising new platform for upconversion†

Debarati Das,[ab] Santosh K. Gupta,[ab]* Reshmi T. Parayil,[ab] B. Modak[bc] and K. Sudarshan[ab]*

Received 16th January 2024,
Accepted 19th February 2024

DOI: 10.1039/d4cp00199k

rsc.li/pccp

Lanthanide-doped luminescent nanoparticles are an appealing system for many applications in the area of biomedical, solar cell, thermometry, anti-counterfeiting, *etc.* due to their sensitivity, reliability, high photochemical stability, and high optical transparency in the visible-NIR range. A color-tunable upconversion-luminescence (UCL) in a new low phonon energy ThO_2 host based on modulating sensitizer concentration has been realized in this work and it may work as a potential candidate to replace corrosive and toxic fluoride based hosts in the future. Er^{3+}–Yb^{3+} co-doped thoria nanoparticles were prepared using a gel combustion route and their structural and luminescence properties were determined as a function of the Yb^{3+} concentration. Phonon dispersion measurements have established the dynamic structural stability of the thoria nanoparticles. Density functional theory (DFT) was used to calculate the defect formation energy, highlighting the feasibility of dual ion (Er^{3+} and Yb^{3+}) doping in thoria. The morphology and average size of the doped thoria was studied using high resolution transmission electron microscopy (HRTEM), and any defects evolving as a result of aliovalent doping were probed using positron annihilation lifetime spectroscopy (PALS). With 980 nm laser excitation, the nanothoria emits green and near-red light. A significant enhancement of the red-to-green intensity ratio of Er^{3+} ions in nanothoria was observed with an increase in Yb^{3+} concentration which resulted in beautiful color tunability from green to yellow light in going from lower (up to ~5 mol%) to higher (10 and 15 mol%) Yb^{3+} concentration. The power dependence and the dynamics of the upconverted emission confirm the existence of two-photon upconversion processes for the green and red emissions.

1. Introduction

Upconversion nanophosphors (UCNPs) are regularly studied in the scientific community owing to their application in many areas encompassing health, energy and the environment.[1–7] Their applicability has been attributed to the conversion of low energy photons to high energy photons exhibiting anti Stoke's shifts and displaying bright emission, lower autofluorescence, deeper penetration, negligible photobleaching, higher photo stability, *etc.*[5,8] The three basic requirements to achieve efficient upconversion luminescent materials are dopant, sensitizer and host matrix. In most of the reported works, Er^{3+}, Ho^{3+} and Tm^{3+} are used as dopant ions whereas Yb^{3+} is used as the sensitizer whenever the pumping energy is 980 nm.[9,10] The choice of sensitizer can vary depending upon the excitation wavelength in the upconversion process, whereas the dopant can also be changed based on the required energy conversion region. Among the lanthanide ions, the Er^{3+}–Yb^{3+} couple is commonly used for realizing efficient upconversion. Fluoride based hosts are considered to be an excellent luminescence host for UC compared to oxides owing to low phonon energy which may lower the non-radiative channels.[11] However, a fluoride based matrix is corrosive in nature and handling them in a normal laboratory set-up may be an issue.[2,12] So there is a huge demand within the scientific community working in the area of upconversion phosphors, to look for inorganic host matrices which stringently fulfil the important and necessary criteria: this includes that the host matrix should be thermally/structurally/chemically stable, should possess a wide band gap, easy to synthesize and exhibit low phonon frequency. In that context ThO_2 is considered an excellent luminescence host owing to its stable crystal structure, high chemical stability, single valence state of cation and low phonon frequency.[13–15]

[a] *Radiochemistry Division, Bhabha Atomic Research Centre, Mumbai-400085, India. E-mail: santoshg@barc.gov.in, kathis@barc.gov.in*
[b] *Homi Bhabha National Institute, Anushaktinagar, Mumbai-400094, India*
[c] *Chemistry Division, Bhabha Atomic Research Centre, Mumbai-400085, India*

† Electronic supplementary information (ESI) available. See DOI: https://doi.org/10.1039/d4cp00199k

The ability to accommodate a large amount of fluorescence active dopant ions in its open calcium fluorite structures (space group $Fm\bar{3}m$) together with superior chemical and mechanical stability are additional benefits. Thorium oxide has shown tremendous potential in the area of electro and photocatalysis, in solid oxide fuel cells (SOFC), sensor materials, photoluminescence host matrix, *etc.*[14,16–24] Despite these advantages, there are absolutely no reports exploring thoria as an upconversion luminescence host.

Lin *et al.* have explored the optical properties of ThO_2 and Eu-doped ThO_2 nanotubes.[25] Harvey and his group on the other hand have explored the thermoluminescence (TL) of undoped and doped ThO_2 [26] whereas our group have also worked on Eu, Dy and Tb doped ThO_2 nanoparticles.[16] Kristianpoller *et al.* have investigated luminescence emitted during X-irradiated (XL) as well as the TL of ThO_2:Ca single crystals.[27] Pandey *et al.* have recently explored bismuth luminescence in thoria and proposed a dual band endowed by oxygen vacancies and Bi^{3+}.[21] Our group has also explored the emission of uranium ions in thoria.[28] But all this work deals with the conversion of high energy photons into low energy ones known as down-conversion luminescence (DCL) which curtails their applicability in the area of bioimaging owing to lower tissue penetration and harmful effects of UV photons. Here in this work for the first time we are exploring the potential of thoria nanoparticles as an Er^{3+}–Yb^{3+} upconversion host. The gel-combustion synthesized[29] UCNPs ThO_2:1%Er^{3+},x%Yb^{3+} (x = 1–15) were characterized using powder X-ray diffraction, Raman spectroscopy and high resolution transmission electron microscopy (HRTEM). With Th^{4+} being tetravalent and the dopant and sensitizer being trivalent in nature; we have probed the defects in such materials due to such aliovalent substitution using positron annihilation lifetime spectroscopy (PALS). Density functional theory (DFT) calculations were also carried out to calculate the phonon frequency of thoria and defect formation energy of doping Er^{3+} and co-doping Er^{3+} and Yb^{3+} in ThO_2.

2. Experimental

2.1. Synthesis

Undoped and Er, Yb codoped ThO_2 nanopowders were synthesized using a gel-combustion method using $Th(NO_3)_4{\cdot}5H_2O$ as the oxidant and urea as the fuel in a 1 : 2 molar ratio using a previous procedure.[13] For doping with Er^{3+} and Yb^{3+}, stock solutions of the respective trivalent ions were prepared by dissolving Er_2O_3 and Yb_2O_3 in conc. HNO_3 and the requisite amounts of the stock solutions were then added to the precursor solution of oxidant and fuel. The schematic depicting the gel-combustion synthesis of Er^{3+}, Yb^{3+} co-doped thoria (YET) upconvertible nanoparticles (UCNPs) is shown in Scheme 1.

2.2. Instrumentation and computation details

X-ray diffraction (XRD) studies of the powder samples of undoped and doped thoria have been carried out on a benchtop X-ray diffractometer (Proto make) in the 2θ range of 15–80° using Cu Kα as the X-ray source. Rietveld refinement was carried out using FullProf software. Raman spectrum was recorded on Seki's STR300 spectrometer with a laser excitation wavelength of 532 nm. TEM, HRTEM and Selected Area Electron Diffraction (SAED) patterns were taken in a field emission transmission electron microscope of JEOL make (2100F model). Positron annihilation lifetime spectra were measured with powder thoria samples under ambient conditions with a lifetime spectrometer having a time resolution of 175 ps. The spectra were analysed using PALSFit software.[30] The UC emission measurements were carried out using an Edinburgh Instruments Fluorimeter of series FLS 1000 which is equipped with both a visible and NIR PMT using a monochromatic diode laser of excitation wavelength 980 nm as the NIR source.

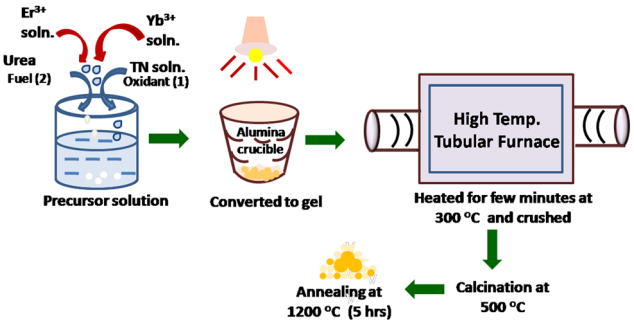

Scheme 1 Schematic showing gel-combustion synthesis of Er^{3+}, Yb^{3+} co-doped thoria UCNPs.

Density of states defect formation energies are calculated using DFT. More details of the calculation methodology are given in section S1 in ESI.†

3. Results and discussion

3.1. Phase analysis, density of states calculations and phonon dispersion

Fig. 1a shows the XRD pattern of undoped and ThO_2:1%Er^{3+},-x%Yb^{3+} (x = 1–15). The entire XRD pattern completely matches with the standard pattern reported for thoria with JCPDS-01-071-6407. None of the samples depicted any impurity peaks suggesting that dopants are occupying the lattice Th^{4+} site. The peaks were marginally shifted to a higher angle with doping. The lattice constants have been calculated *via* Rietveld analysis. The typical Rietveld fitted spectra are shown in Fig. 1b. All the Rietveld fitted spectra and corresponding data are shown in Fig. S1 and Table S1 of ESI.† The lattice parameters obtained are shown in the Fig. 1c and the reduction in unit cell lattice parameter with doping is in line with the ionic radii of the dopants being smaller than Th^{4+}. Further, the crystallite sizes were calculated using the Debye Scherrer equation (see S2 of ESI,† for details) and are listed in Table 1. All the samples are nano sized and smaller than 25 nm. But interestingly crystallite size decreases monotonically from ~24.4 to 11.8 nm with an increase in doping suggesting hindrance to the crystallite growth. This is also in sync with TEM results where the average

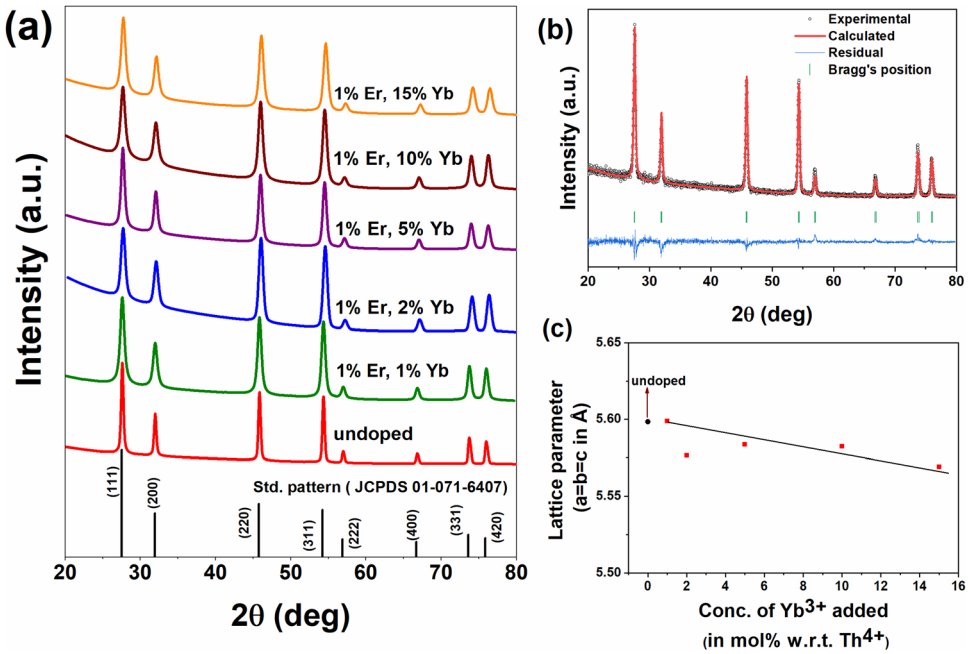

Fig. 1 (a) XRD pattern of ThO_2:1%Er^{3+},*x*%Yb^{3+} nanophosphor (*x* = 1, 2, 5, 10 and 15), (b) typical Rietveld fitting of the spectrum, (c) variation of lattice parameters with doping.

Table 1 Crystallite size of nanostructure ThO_2:1%Er^{3+},*x*%Yb^{3+} (*x* = 1–15)

Dopant concentration in ThO_2 sample	Crystallite size (nm)
1%Er+1%Yb	24.4
1%Er+2%Yb	14.4
1%Er+5%Yb	13.2
1%Er+10%Yb	12.2
1%Er+15%Yb	11.8

particle size at 1% Yb^{3+} doping was 51 nm and it reduces to 28 nm when Yb^{3+} doping is raised to 15%.

All the DFT calculations have been carried out using the fluorite type structure of ThO_2 (space group: $Fm\bar{3}m$, No. 225) (Fig. S2, ESI†). The calculated cell parameter was found to be 5.6158 Å, which is very close to the experimentally reported value.[31,32] The calculated band gap under the HSE level of calculation is found to be 6 eV, which is in excellent agreement with the experimentally observed value.[33] This justifies the choice of the present computational parameters. Fig. 2a shows the density of states (DOS) of ThO_2, which indicates that the valence band maximum (VBM) is dominated by O p states, with a small contribution from Th d and f states. On the other hand, the conduction band minimum (CBM) is contributed by Th f states along with a small contribution from the Th d and O p states. Fig. 2b shows the phonon dispersion curve for ThO_2 calculated within the GGA level along the high symmetric directions of *Γ_X_W_Γ_L*. It can be observed that no imaginary frequencies were obtained, indicating that the ThO_2 structure is dynamically stable.

3.2. Doping Efficacy of Yb^{3+} and Er^{3+} ion in ThO_2

Now we proceed to investigate the role of doping with Yb and Er into ThO_2. To model the (Er,Yb)-doped ThO_2, we have chosen a 96 atoms cell, and replaced one of the Th atoms with Er/Yb. For (Er,Yb)-doped ThO_2, we have considered two different structures by varying the relative distance between Yb and Er. Both the structures are energetically close to each other. The defect formation energies have been calculated using the mathematical relationship:[34,35]

$$E_{\text{formation}} = E_{\text{defect}} - E_{\text{perfect}} + q\sum n_X \mu_X \quad (1)$$

where, E_{defect} and E_{perfect} indicate the energies of the doped and perfect ThO_2, respectively, calculated with a similar cell size, μ_X is the chemical potential of the element X and n_X indicates the number of elements added ($q = -1$) or removed ($q = +1$) to generate the doped system. The variation of defect formation energies for the doping of Yb/Er into ThO_2 as a function of host chemical potential are shown in the Fig. 3. It can be observed that doping of both Yb and Er is more favorable in Th-poor condition. Interestingly, the defect formation energy is found to be reduced significantly for the cases of (Er,Yb)-doped ThO_2 under Th-poor condition. This indicates that the formation of the (Er,Yb)-doped ThO_2 is energetically more feasible (under Th-poor condition) than the doping with individual elements.

3.3. Transmission electron microscopy

TEM images of the representative ThO_2:1%Er^{3+},*x*%Yb^{3+} (*x* = 1, 5 and 15) are shown respectively in Fig. 4a, d and g. The formation of nanoparticles is clearly seen from these TEM images though the particles are slightly aggregated. This could be due to the large heat of combustion generated during the combustion reaction involving precursors and the fuel. We have further calculated the average size of these nanoparticles using ImageJ software and the values are 51, 47 and

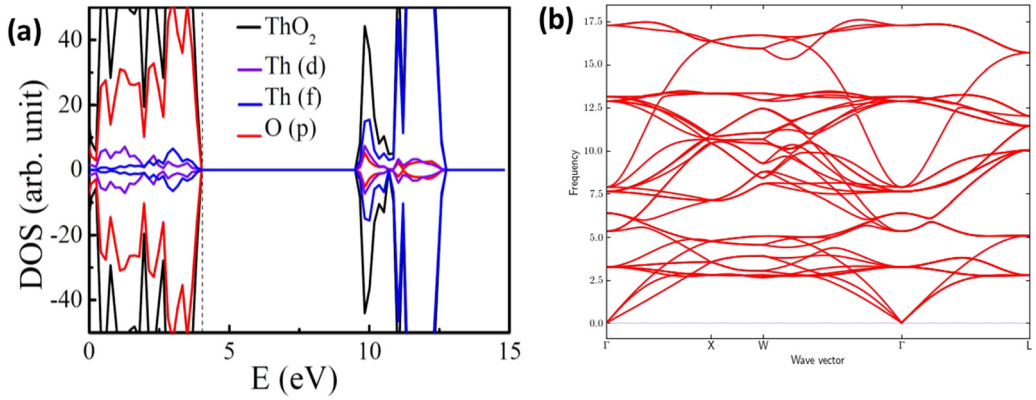

Fig. 2 (a) Density of states of ThO_2. The vertical dashed line indicates the Fermi level. (b) Phonon dispersion curve for ThO_2 calculated within the GGA level where the frequency is in THz.

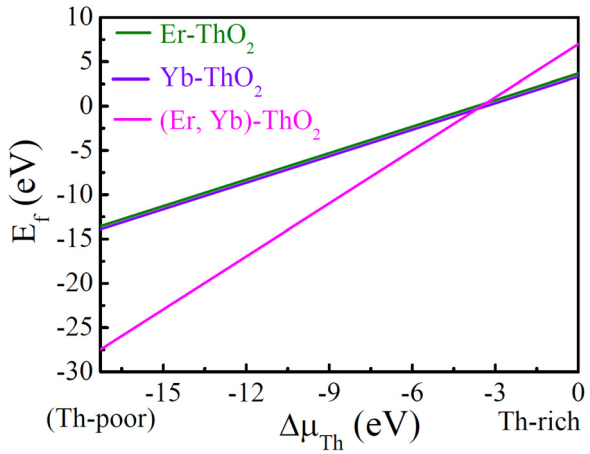

Fig. 3 Variation of defect formation energies for the doped ThO_2.

28 nm respectively for 1, 5 and 15% Yb^{3+} doping. Reduction in crystallite size with higher Yb^{3+} doping was also evident from the XRD as discussed earlier. The HRTEM images of ThO_2:1%Er^{3+},*x*%Yb^{3+} (*x* = 1, 5 and 15) are shown respectively in Fig. 4b, e and h which clearly show the lattice fringes. The interplanar distance was obtained as 0.320 and 0.281 nm which corresponds to the (111) and (200) crystal planes in fluorite structured ThO_2.[18] The selected area electron diffraction (SAED) patterns shown respectively in Fig. 4c, f and i, confirm the formation of cubic phase ThO_2, and the ring patterns depict the high crystallinity of doped thoria nanoparticles. The crystal planes corresponding to the diffraction spots are marked in the figure.[15]

3.4. Raman spectroscopy

Fig. 5 shows the Raman spectra of ThO_2:1%Er^{3+},*x*%Yb^{3+} (*x* = 1–15) UCNPs. For pure thoria, a single peak in the range 460–465 cm^{-1} corresponds to the T_{2g} stoichiometric fluorite structure of ThO_2, and is well reported.[13] In the present case, this peak is at 465 cm^{-1} in the samples with lower dopant concentration and is marginally red shifted when the dopant concentration is very high. Such a shift with dopants of different ionic radii is known in other fluorite structures like CeO_2. The other bands are mostly due to defects induced by doping with trivalent lanthanides which differ in size as well as charge, that leads to charge compensating vacancies. The Raman peaks are broader in samples with higher dopant concentration showing the increased disorder in the system. The band around 500 cm^{-1} might be from oxygen vacancies. In general, the band from oxygen vacancies in thoria is reported in the range 550–580 cm^{-1} and here, though speculative, it appears that the oxygen vacancies are associated with the trivalent dopants more and might form RE-Vo-RE type vacancy complexes. The Raman peak around 625 cm^{-1} is due to REO_8 type complexes whose intensity relative to the peak at 500 cm^{-1} is reduced, due to enhanced oxygen vacancy formation.[36] The other bands are similar to those reported in the defect induced Raman spectra of ThO_2 and CeO_2.[37,38]

3.5. Positron annihilation lifetime spectroscopy

The positron lifetime spectra was fitted to three lifetime components as depicted in Fig. 6A and the intensity of the third component was less than 0.5%. For the other two lifetimes, the corresponding intensities and the average lifetime are given in Fig. 6B. The first positron lifetime arises due to positron annihilation in the bulk. The first positron lifetime (τ_1) in undoped thorium oxide is 192 ps. A positron lifetime of 184 ps with 88% intensity was reported by Upadhyaya *et al.*[39] in sintered thoria. The lifetime is marginally higher in the present case and the contribution to this lifetime from annihilations in oxygen vacancies could be responsible for this. The second lifetime component is due to vacancy clusters near the surface. Upon initial doping with Er and Yb, the intensity of the second positron lifetime component drastically increased from 15% to 26% showing the formation of vacancy defects near the surfaces. The XRD patterns suggest reduced crystallinity in the doped samples and this would facilitate the positron reaching the surface of the crystallites increasing this intensity. With higher doping of trivalent lanthanides, the first positron lifetime component increased and the fraction of positrons

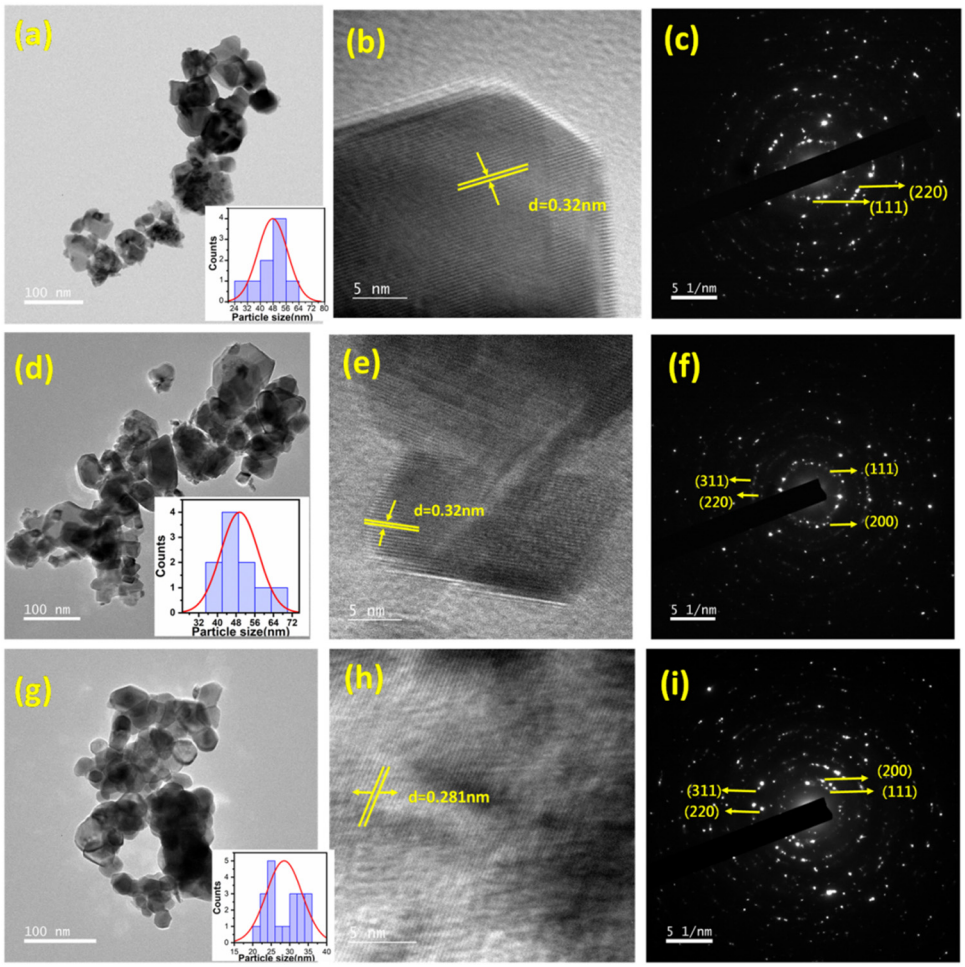

Fig. 4 (a), (d) and (g) TEM images, (b), (e) and (h) HRTEM images and (c), (f) and (i) SAED patterns of ThO_2:1%Er^{3+},*X*%Yb^{3+} (*X* = 1, 5 and 15) UCNPs.

reaching the surface states reduced due to the enhanced concentration of isolated oxygen in the bulk as can be seen from Fig. 6B and also supported by the increased intensity of the 500 cm^{-1} peak in the Raman spectra. The magnitude of the second lifetime suggests that the size of the vacancy cluster increased, or with higher doping, the number of oxygen vacancies agglomerating near the surface increased.

3.6. Upconversion photoluminescence spectroscopy

The UC emission spectra in the visible region for a series of ThO_2:1%Er^{3+},*x*%Yb^{3+} (*x* = 1, 2, 5, 10 and 15 mol%) samples under 980 nm diode laser pumping is shown in Fig. 7a. The emission spectra depict an intense green (530–550 nm) and red (670 nm) emission bands, with the former having relatively higher intensity than the latter up to 5 mol% Yb^{3+} doping, and situation reverses when sensitizer doping is 10 and 15%. This is explained in detail later in this section. These peaks are ascribed to $^2H_{11/2} \rightarrow {}^4I1_{5/2}$ (~530 nm), $^4S_{3/2} \rightarrow {}^4I1_{5/2}$ (~550 nm) and $^4F_{9/2} \rightarrow {}^4I1_{5/2}$ (~670 nm) transitions of the trivalent erbium ion. An enlarged version of the 5–10% Yb^{3+} co-doped samples UC spectra is shown in Fig. 7b for better visualization. Severe stark splitting of these electronic levels is evident from the UC emission spectra which could be attributed to the crystalline local field of the cubic thorium oxide with defect fluorite structure. The visible emission here on absorption of 980 nm photons, arises through energy transfer from the Yb^{3+} (sensitizer) to the Er^{3+} (dopant) promoting electrons from the ground to the various excited states. Also, the emission intensity of the UC phosphor was investigated with varying Yb^{3+} ion concentration wherein the Er^{3+} concentration was fixed at 1 mol%, and the concentration of the Yb^{3+} ion was changed from 1 to 15 mol%. But to our surprise at 2.0 mol% concentration, quenching happened. This can be seen from Fig. 7c which clearly depicts the monotonic reduction in overall upconversion intensity (for both green and red bands) as a function of Yb^{3+} concentration. This could be understood by taking into account two phenomenon which are happening beyond 1.0 mol%: (A) at higher concentration of Yb^{3+} ions, the large photon flux of 980 nm wavelength will be absorbed and more energy transferred by excited photons; and (B) at higher Yb^{3+} doping levels it can act as a trapping level and dissipate energy through non-radiative pathways. So here the concentration quenching happening beyond 1.0 mol% of Yb^{3+} ions is ascribed to process (B) which may be more dominant

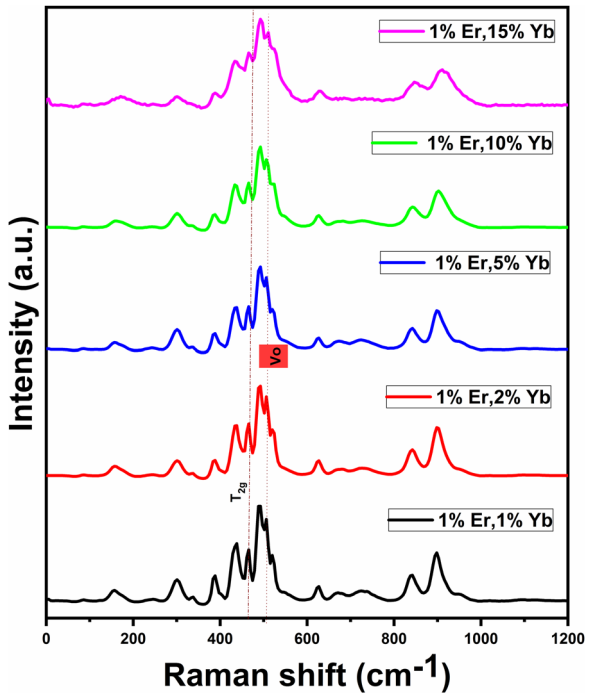

Fig. 5 Raman spectra of ThO_2:1%Er^{3+},*x*%Yb^{3+} nanophosphor (*x* = 1, 2, 5, 10 and 15).

than process A. The other possible reason could be higher density of creation of charge, compensating the defects from aliovalent substitution of Yb^{3+} on Th^{4+} site in the form of oxygen vacancies which may provide additional pathways for non-radiative transitions and degrade the upconversion intensity. This proportionally increases with increasing Yb^{3+} concentration and the formation of oxygen vacancies is well supported by the positron annihilation lifetime spectroscopy results.

The red to green ratio (R/G) is very informative in terms of designing color tunable UC phosphors. Here in this case we have also calculated the R/G ratio at different Yb^{3+} concentrations and plotted the same in Fig. 8a. Interestingly it was seen that in the lower concentration domain of the Yb^{3+} ion of 1–5%; the green intensity was overpowering the red emission (red and black UC spectra in the lower left side inset) whereas at 10–15%; the red intensity is much higher than the green intensity (green and pink UC spectra in the top right side inset).

Based on earlier publications on phosphor with lower doping levels of sensitizer; Yb^{3+} ions find it difficult to substantially populate $^4I_{11/2}$ and $^4F_{7/2}$ energy levels,[40] therefore, the excited Er^{3+} ions occupying $^4F_{7/2}$ level will prefer to relax to the mixed $^2H_{11/2}$ + $^4S_{3/2}$ states leading to more green emission than the red ones. This can be clearly seen from Fig. 8a in the R/G plot as well as UC spectral plots. However, when Yb^{3+} concentrations exceed 5.0 mol%, the mechanism of UC emission changes. At higher sensitizer doping, the Yb^{3+} → Er^{3+} energy transfer process becomes more facile to populate the excited levels of trivalent erbium ions, providing an additional pathway for cross relaxation (CR1) to populate preferably the $^4F_{9/2}$ level associated with the red UC band. This CR1 pathways would be: Er^{3+} ($^4F_{7/2}$) + Er^{3+} ($^4I_{11/2}$) → Er^{3+} ($^4F_{9/2}$) + Er^{3+} ($^4F_{9/2}$)[41] which would lead to enhanced red UC emission with respect to green emission bands in thoria nanoparticles.

The beautiful color tuning in ThO_2:1%Er^{3+},*x*%Yb^{3+} nanophosphor (*x* = 1, 2, 5, 10 and 15) as a function of Yb^{3+} concentration is also perceived in the value of color coordinates evaluated and mentioned in Table S2 (ESI†). It can be seen from this table that the values are quite different in the lower Yb^{3+} concentration regime (1–5%) and higher Yb^{3+} concentration (10 and 15%). The chromaticity diagram of these nanophosphors at different Yb^{3+} concentrations is shown in Fig. 8b. It can be clearly seen that color is tuned from green in the lower Yb^{3+} concentration regime (1–5%) to yellow at Yb^{3+} concentration (10 and 15%).

3.7. Pump power dependent upconversion

For studying the UC mechanism involved in the materials, the pump power dependence on two of the representative samples ThO_2:1%Er^{3+},1%Yb^{3+} and ThO_2:1%Er^{3+},15%Yb^{3+} has been carried out. The number of photons involved in the UC emission was obtained from the following relation:[6]

$$I_{UC} \propto P_{Ex}^{n} \quad (2)$$

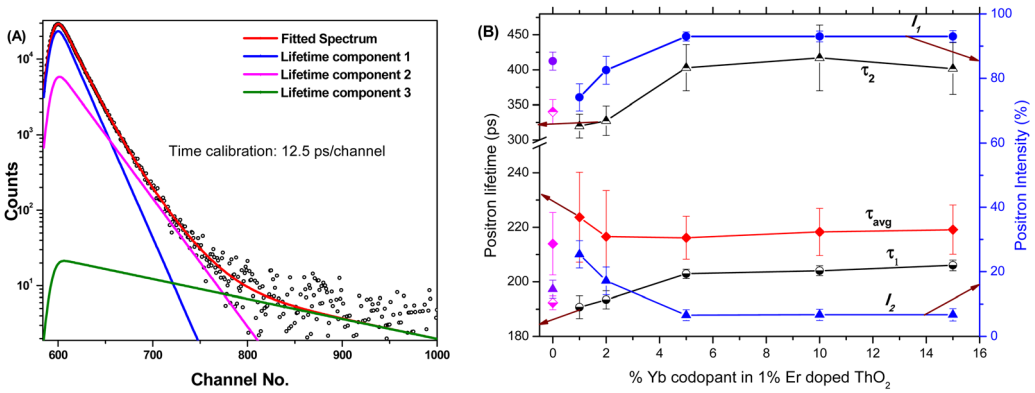

Fig. 6 (A) Typical fitting of PAL spectrum showing extraction of the positron lifetimes (B) positron lifetimes and intensities in doped thoria samples, the data corresponding to undoped thoria are shown at *x*-coordinate of '0'.

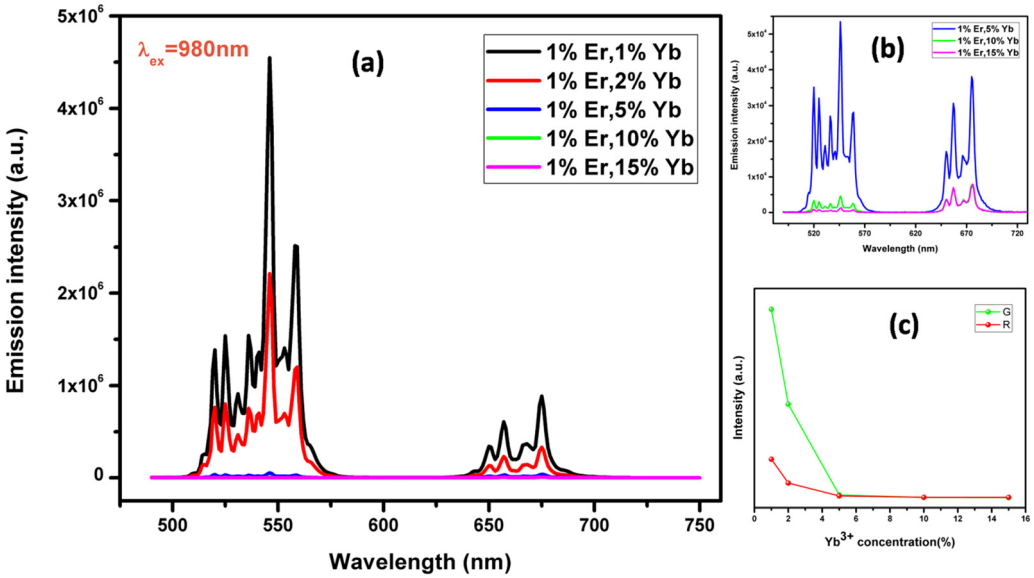

Fig. 7 (a) UC emission spectra, (b) magnified UC spectra of ThO_2:1%Er^{3+},*x*%Yb^{3+} nanophosphor with *x* = 5, 10 and 15 and (c) variation of red and green emission intensity with Yb^{3+} concentrations, ThO_2:1%Er^{3+},*x*%Yb^{3+} nanophosphor (*x* = 1, 2, 5, 10 and 15).

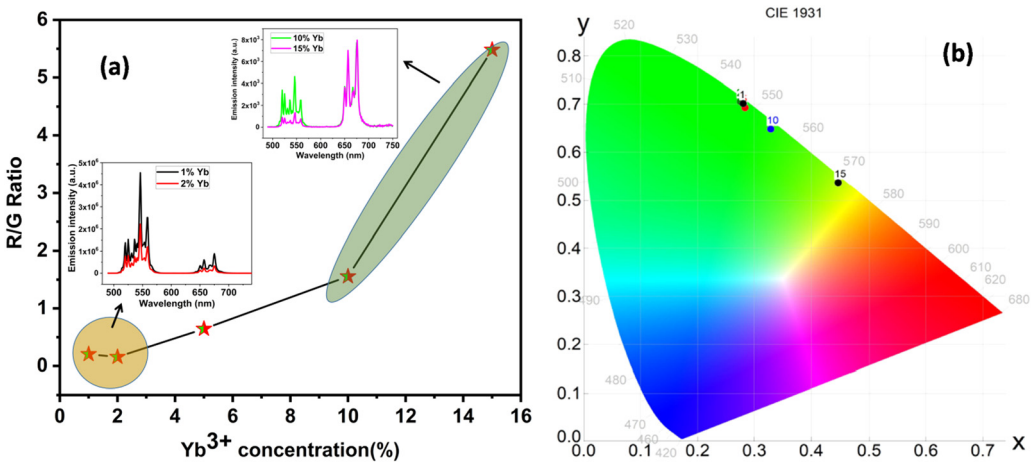

Fig. 8 (a) Variation of red to green emission ratio. Insets show UC spectra in the low and high concentration regions of Yb^{3+} sensitizer, and (b) color coordinate diagram depicting variation in CIE values with Yb^{3+} concentrations of ThO_2:1%Er^{3+},*X*%Yb^{3+} nanophosphor (*x* = 1, 2, 5, 10 and 15).

where I_{UC} represents the intensity of UCL, P_{Ex} is the excitation power and *n* is the number of photons involved in the UC process. Fig. 9a shows the UC emission spectra of ThO_2:1%Er^{3+}, 1%Yb^{3+} with different laser power starting from 310 to 2820 mW. With an increase in laser power the emission intensity is also increased up to 2200 mW. It can be seen that green emission is dominant compared to red emission in this particular composition of Yb and Er at all laser powers. Fig. 9b shows the UC emission spectra of ThO_2:1%Er^{3+},15%Yb^{3+} with different laser power starting from 310 to 2820 mW and here the red emission is dominant over the green emission. This can be explained on the basis of the cross relaxation mechanism $^4F_{7/2} + {}^4I_{11/2} \rightarrow {}^4F_{9/2} + {}^4F_{9/2}$ which increases the $^4F_{9/2}$ level population,[42] as discussed earlier. With an increase in the laser power the emission intensity enhanced up to 651 mW, after which a reduction in intensity was observed. The reduction in UC emission intensity at elevated pump power is ascribed to laser induced heating which enhances the multiphonon relaxation rate and causes a reduction in the radiative transitions.[43]

The log–log plot of laser excitation power and integrated emission intensity is shown in Fig. 9c. It can be seen that the number of photons (*n*) involved in the UC process is obtained as 1.52 and 1.66 for green and red emission which is much higher than 1, so the upconversion in thoria nanoparticles is a biphotonic process. In this two-photon UC, the green emitting levels $^2H_{11/2}$ and $^4S_{3/2}$, are populated through the energy transfer upconversion mechanism, whereas the red emitting state, $^4F_{9/2}$, is subsequently populated *via* $^2H_{11/2}$, $^4S_{3/2} \rightarrow {}^4F_{9/2}$ multiphonon relaxation. The decrease in the slope value at higher laser power is also explained by Nascimento *et al.*[44] Due to competition between linear decay and the UC process,

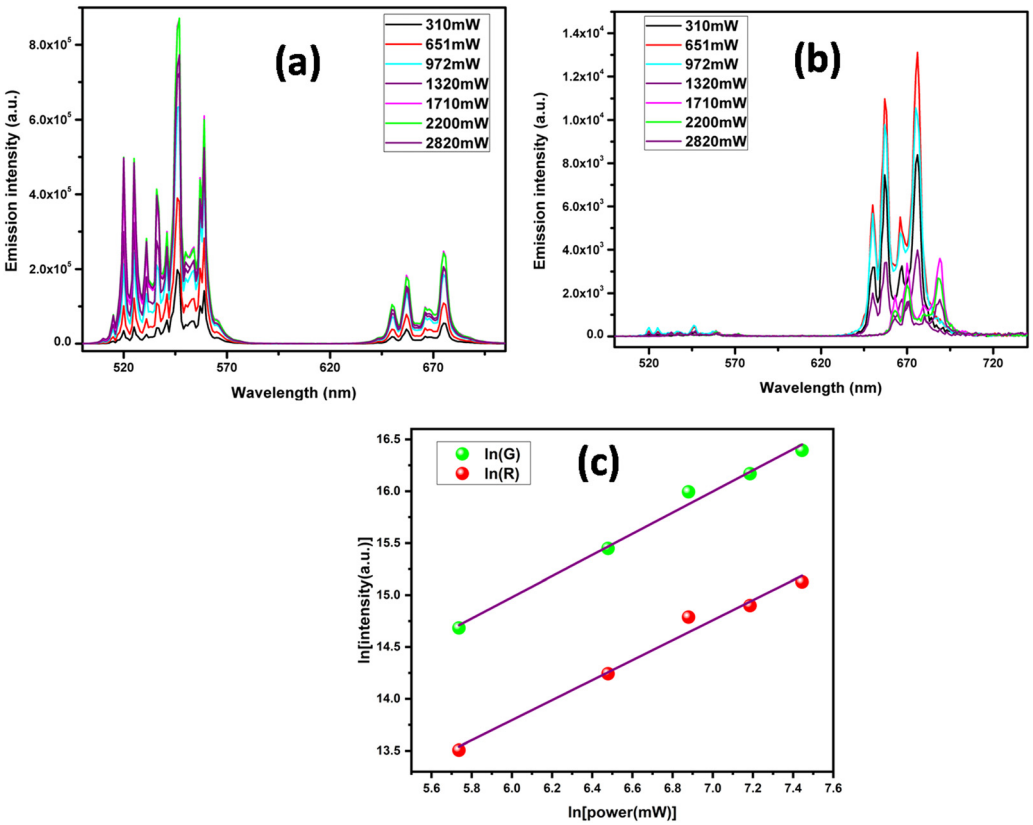

Fig. 9 UC emission spectra of (a) ThO_2:1%Er^{3+},1%Yb^{3+}, (b) ThO_2:1%Er^{3+},15%Yb^{3+} and (c) dependence of pump power on green and red emission in ThO_2:1%Er^{3+},1%Yb^{3+}.

saturation effects dominate at higher laser power which reflects in the reduction of slope value.

Fig. 10 represents the decay curve of ThO_2:1%Er^{3+},x%Yb^{3+} (x = 1, 3, 5, 10 and 15) samples with an excitation wavelength of 980 nm and emission wavelength of 676 nm. The decay follows a bi-exponential decay as in the following equation:[45]

$$I = A_0 + A_1 \exp(-t/T_1) + A_2 \exp(-t/T_2) \quad (3)$$

where T_1 and T_2 are the lifetime of the fast and slowly decaying components, respectively, A_1 and A_2 are the fitting parameters and A_0 is the background or zero-offset. The fitted lifetime values are shown in Table S3 of ESI.† Inset of Fig. 10 shows the variation in average fluorescence lifetimes with Yb concentration. It can be seen that with increasing concentration of Yb^{3+} from 1.0 to 2.0 mol% the lifetime value also increases. With further increase in the concentration of Yb^{3+} beyond 2.0 mol% the lifetime value reduces. This suggests that the UC luminescence lifetime of the selected red emissions exhibit a decreasing trend with the increase in sensitizer concentration beyond 2.0 mol%. This photophysical process indicated that increasing Yb^{3+} concentration may invoke an additional mechanism to quench $^4S_{3/2}$ and $^4F_{9/2}$ transition emission. This observation can be explained on the basis of back energy transfer (BET) from Er^{3+} to Yb^{3+}. After excitation, the $^4F_{7/2}$ and $^2H_{11/2}$ of Er^{3+} can transfer energy to Yb^{3+} ions in the ground state and on increasing the concentration of Yb^{3+}, the back energy transfer become stronger and leads to the reduction in the lifetime value.[40]

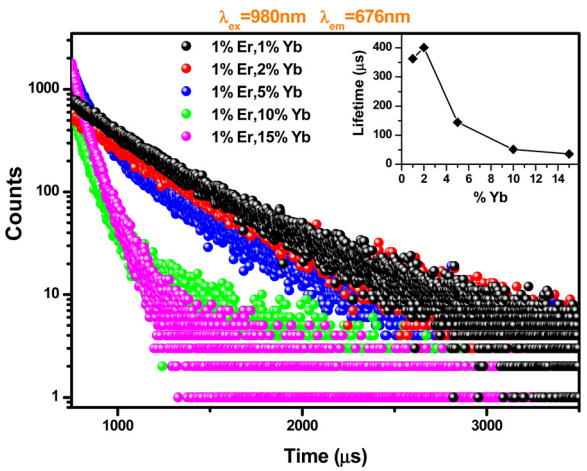

Fig. 10 UC luminescence decay profile of ThO_2:1%Er^{3+},x%Yb^{3+} nanophosphor (x = 1, 2, 5, 10 and 15). Inset shows the variation in average fluorescence lifetimes with Yb doping.

4. Conclusion

A color-tunable upconversion-luminescence in a new low phonon energy ThO_2 host based on modulating sensitizer concentration

has been realized in this work. The high dynamic stability of the thoria structure is validated using phonon dispersion calculation. ThO_2 doped with Er^{3+} and varying concentrations of Yb^{3+} ions have been synthesized using the gel-combustions route. DFT calculated defect formation energy shows that doping with both these ions is highly energetically favourable in thoria. The phase purity and the crystal structures have been characterized by powder XRD and Raman spectroscopy. TEM images show the formation of spherical nanoparticles in the size domain ~20–50 nm. Raman spectroscopy and PALS have suggested enhanced oxygen vacancy formation at higher Yb^{3+} concentrations which lead to a reduction in UCL intensity at concentrations higher than 1% Yb^{3+}. The oxygen vacancies are associated with the trivalent dopants more and might form RE-Vo-RE type vacancy complexes. With 980 nm laser excitation, color-tunable UC luminescence from green to yellow was easily achieved by tuning the doping concentration of Yb^{3+} from 1.0 to 15% in the system ThO_2:1%Er^{3+},*x*%Yb^{3+}. Based on the UCL dependence on the laser power, both the green and red emission band could be attributed to two-phonon absorption. Our work suggests that thoria can be utilized for other upconverting rare earth ions with improved color hue and brightness and can be potential materials for UC based white lighting and optoelectronic devices.

Conflicts of interest

There are no conflicts of interest to declare.

Acknowledgements

The authors would like to thank Achal S. Kumar from IIT Guwahati for his help in TEM measurements and Dr Rajesh V. Pai from FCD, BARC for providing thorium nitrate stock solutions. The research was funded by the Government of India through the Department of Atomic Energy, India.

References

1 A. Balhara, S. K. Gupta, N. Aggarwal, S. Srivastava, J. J. Panda, S. Patra, A. Chakraborty, S. Rakshit and R. Chakravarty, Remarkably enhanced upconversion luminescence in Na^+ codoped spinel nanoparticles for photothermal cancer therapy and SPECT imaging, *Mater. Adv.*, 2023, **4**(21), 5338–5352.

2 A. Balhara, S. K. Gupta, A. K. Debnath and K. Sudarshan, Utilizing Energy Transfer in Mn2+/Ho3+/$Yb3^+$ Tri-doped ZnAl2O4 Nanophosphors for Tunable Luminescence and Highly Sensitive Visual Cryogenic Thermometry, *ACS Omega*, 2023, **8**(33), 30459–30473.

3 S. Borse, R. Rafique, Z. Murthy, T. J. Park and S. K. Kailasa, Applications of upconversion nanoparticles in analytical and biomedical sciences: a review, *Analyst*, 2022, **147**(14), 3155–3179.

4 H. Chen, B. Ding and J. Lin, Recent progress in upconversion nanomaterials for emerging optical biological applications, *Adv. Drug Delivery Rev.*, 2022, **188**, 114414.

5 J. Huang, L. Yan, S. Liu, L. Tao and B. Zhou, Expanding the toolbox of photon upconversion for emerging frontier applications, *Mater. Horiz.*, 2022, **9**(4), 1167–1195.

6 R. T. Parayil, S. K. Gupta, M. M. Upadhyay, K. Sudarshan and M. Mohapatra, Tunable upconversion in $ZnAl_{2-x}Ga_x$-O_4:Er,Yb phosphors by modulating the Al/Ga ratio and application in optical thermometry, *New J. Chem.*, 2023, 20286–20297.

7 B. S. Richards, D. Hudry, D. Busko, A. Turshatov and I. A. Howard, Photon upconversion for photovoltaics and photocatalysis: a critical review: focus review, *Chem. Rev.*, 2021, **121**(15), 9165–9195.

8 S. K. Gupta, K. Sudarshan and R. M. Kadam, Optical nanomaterials with focus on rare earth doped oxide: a review, *Mater. Today Commun.*, 2021, **27**, 102277.

9 K. Li, D. Zhu and H. Lian, Up-conversion luminescence and optical temperature sensing properties in novel $KBaY(MoO_4)_3$:Yb^{3+},Er^{3+} materials for temperature sensors, *J. Alloys Compd.*, 2020, **816**, 152554.

10 K. Li, D. Zhu and C. Yue, Exceptional low-temperature fluorescence sensing properties in novel $KBaY(MoO_4)_3$:Yb^{3+},Ho^{3+} materials based on FIR of Ho^{3+} transitions $^5F_5(1) \rightarrow {}^5I_8/{}^5S_2 \rightarrow {}^5I_8$, *J. Mater. Chem. C*, 2022, **10**(17), 6603–6610.

11 M. Pokhrel, S. K. Gupta, A. Perez, B. Modak, P. Modak, L. A. Lewis and Y. Mao, Up- and Down-Convertible LaF_3:-Yb,Er Nanocrystals with a Broad Emission Window from 350 nm to 2.8 μm: Implications for Lighting Applications, *ACS Appl. Nano Mater.*, 2021, **4**(12), 13562–13572.

12 A. Balhara, S. K. Gupta, N. Aggarwal, S. Srivastava, J. J. Panda, S. Patra, A. Chakraborty, S. Rakshit and R. Chakravarty, Remarkably enhanced upconversion luminescence in Na^+ codoped spinel nanoparticles for photothermal cancer therapy and SPECT imaging, *Mater. Adv.*, 2023, 5338–5352.

13 D. Das, R. Gupta, S. K. Gupta, A. K. Yadav and K. Sudarshan, Tailoring oxygen vacancies in ThO_2 for improved light emission and ORR electrocatalysis, *Mater. Today Chem.*, 2023, **32**, 101635.

14 S. K. Gupta, M. K. Bhide, S. V. Godbole and V. Natarajan, Probing Site Symmetry Around Eu^{3+} in Nanocrystalline ThO_2 Using Time Resolved Emission Spectroscopy, *J. Am. Ceram. Soc.*, 2014, **97**(11), 3694–3701.

15 T. V. Plakhova, A. Y. Romanchuk, D. V. Likhosherstova, A. E. Baranchikov, P. V. Dorovatovskii, R. D. Svetogorov, T. B. Shatalova, T. B. Egorova, A. L. Trigub, K. O. Kvashnina, V. K. Ivanov and S. N. Kalmykov, Size Effects in Nanocrystalline Thoria, *J. Phys. Chem. C*, 2019, **123**(37), 23167–23176.

16 S. K. Gupta, P. S. Ghosh, A. Arya and V. Natarajan, Origin of blue emission in ThO_2 nanorods: exploring it as a host for photoluminescence of Eu^{3+}, Tb^{3+} and Dy^{3+}, *RSC Adv.*, 2014, **4**(93), 51244–51255.

17 S. K. Gupta, R. Gupta, V. Natarajan and S. V. Godbole, Warm white light emitting ThO_2:Sm^{3+} nanorods: cationic surfactant

assisted reverse micellar synthesis and Photoluminescence properties, *Mater. Res. Bull.*, 2014, **49**, 297–301.
18 C. Diaz, M. L. Valenzuela, M. A. Laguna-Bercero, D. Carrillo, M. Segovia, K. Mendoza and P. Cartes, Solventless Preparation of Thoria and Its Inclusion into SiO_2 and TiO_2: A Luminescence and Photocatalysis Study, *ACS Omega*, 2021, **6**(14), 9391–9400.
19 M. Gabard, Y. Cherkaski, N. Clavier, L. Brissonneau, M. C. Steil, J. Fouletier, A. Mesbah and N. Dacheux, Preparation, characterization and sintering of yttrium-doped ThO_2 for oxygen sensors applications, *J. Alloys Compd.*, 2016, **689**, 374–382.
20 B. Nollet, M. Hvasta, M. Anderson, D. Morgan and J. Schneider, Development of an electrochemical oxygen sensor for liquid sodium using a yttria stabilized zirconia electrolyte, *J. Electrochem. Soc.*, 2017, **164**(2), B10.
21 J. Pandey, A. Sethi, S. Uma and R. Nagarajan, Catalytic Application of Oxygen Vacancies Induced by Bi^{3+} Incorporation in ThO_2 Samples Obtained by Solution Combustion Synthesis, *ACS Omega*, 2018, **3**(7), 7171–7181.
22 F. Pereira, M. Castro, M. Vázquez, L. Debán and A. Aller, Optical properties of ThO_2–based nanoparticles, *J. Lumin.*, 2017, **184**, 169–178.
23 A. Sethi, S. Uma and R. Nagarajan, Oxygen ion conductivity studies of bismuth and bismuth-calcium co-doped ThO_2, *Ceram. Int.*, 2021, **47**(15), 21498–21508.
24 Y. Xue, D. Pan, F. Zuo, S. Xiao, X. Li, F. Lou, M. Li and Y. Ouyang, Improved performance of self-reactivated Pt–ThO_2/C catalysts in a direct ethanol fuel cell, *RSC Adv.*, 2022, **12**(27), 17012–17019.
25 Z.-W. Lin, Q. Kuang, W. Lian, Z.-Y. Jiang, Z.-X. Xie, R.-B. Huang and L.-S. Zheng, Preparation and Optical Properties of ThO_2 and Eu-Doped ThO_2 Nanotubes by the Sol–Gel Method Combined with Porous Anodic Aluminum Oxide Template, *J. Phys. Chem. B*, 2006, **110**(46), 23007–23011.
26 P. J. Harvey and J. B. Hallett, Thermoluminescence of pure and doped ThO_2, *J. Lumin.*, 1976, **14**(2), 131–146.
27 N. Kristianpoller and A. Rehavi, Luminescence and defects in Ca^{2+} doped thoria crystals, *J. Lumin.*, 1984, **31**, 176–178.
28 S. K. Gupta, N. Pathak and R. M. Kadam, Probing local coordination and oxidation state of uranium in ThO_2:U nanostructured, *J. Mol. Struct.*, 2015, **1102**, 81–85.
29 S. K. Gupta, M. Mohapatra, V. Natarajan and S. V. Godbole, Photoluminescence Investigations of the Near White Light Emitting Perovskite Ceramic $SrZrO_3$:Dy^{3+} Prepared Via Gel-Combustion Route, *Int. J. Appl. Ceram. Technol.*, 2013, **10**(4), 593–602.
30 J. V. Olsen, P. Kirkegaard, N. J. Pedersen and M. Eldrup, PALSfit: a new program for the evaluation of positron lifetime spectra, *Phys. Status Solidi C*, 2007, **4**(10), 4004–4006.
31 H. Leigh and E. McCartney, Redetermination of lattice parameter of ThO_2, *J. Am. Ceram. Soc.*, 1974, **57**(4), 192.
32 M. Singh, T. Kumagai and A. El-Azab, A first-principles investigation of point defect structure and energetics in ThO_2, *J. Appl. Phys.*, 2022, **132**(13), 135111.
33 E. T. Rodine and P. L. Land, Electronic Defect Structure of Single-Crystal ThO_2 by Thermoluminescence, *Phys. Rev. B: Solid State*, 1971, **4**(8), 2701–2724.
34 P. Modak and B. Modak, Exploring the role of vacancy defects in the optical properties of $LiMgPO_4$, *Phys. Chem. Chem. Phys.*, 2020, **22**(28), 16244–16257.
35 P. Modak and B. Modak, Electronic structure investigation of intrinsic and extrinsic defects in LiF, *Comput. Mater. Sci.*, 2022, **202**, 110977.
36 C. Nandi, M. Shafeeq, S. Kesari, R. Rao, V. Grover, A. Prakash and A. K. Tyagi, Structural and thermal expansion studies in ternary ThO_2–CeO_2–$NdO_{1.5}$ system: mimicking actinide substituted ThO_2, *J. Nucl. Mater.*, 2019, **520**, 226–234.
37 K. Rickert, T. A. Prusnick, E. Hunt, A. French, D. B. Turner, C. A. Dennett, L. Shao and J. M. Mann, Raman and photoluminescence evaluation of ion-induced damage uniformity in ThO_2, *Nucl. Instrum. Methods Phys. Res., Sect. B*, 2022, **515**, 69–79.
38 A. Westermann, C. Geantet, P. Vernoux and S. Loridant, Defects band enhanced by resonance Raman effect in praseodymium doped CeO_2, *J. Raman Spectrosc.*, 2016, **47**(10), 1276–1279.
39 D. Upadhyaya, R. Muraleedharan, B. Sharma and K. Prasad, Positron lifetime studies on thorium oxide powders, *Philos. Mag. A*, 1982, **45**(3), 509–518.
40 C. Mi, J. Wu, Y. Yang, B. Han and J. Wei, Efficient upconversion luminescence from $Ba_5Gd_8Zn_4O_{21}$:Yb^{3+},Er^{3+} based on a demonstrated cross-relaxation process, *Sci. Rep.*, 2016, **6**(1), 22545.
41 D. Chavez, C. R. Garcia, J. Oliva, E. Montes, A. I. Mtz-Enriquez, M. A. Garcia-Lobato and L. A. Diaz-Torres, Effect of Yb^{3+} concentration on the green-yellow upconversion emission of $SrGe_4O_9$:Er^{3+} phosphors, *Ceram. Int.*, 2019, **45**(14), 16911–16917.
42 F. Vetrone, J.-C. Boyer, J. A. Capobianco, A. Speghini and M. Bettinelli, Significance of Yb^{3+} concentration on the upconversion mechanisms in codoped Y_2O_3:Er^{3+},Yb^{3+} nanocrystals, *J. Appl. Phys.*, 2004, **96**(1), 661–667.
43 S. H. Nannuri, A. R. Samal, C. K. Subash, C. Santhosh and S. D. George, Tuning of structural, laser power-dependent and temperature dependent luminescence properties of $NaYF_4$:Yb,Er (Y: 88%, Yb: 10 and Er: 2%) submicron crystals using Cr^{3+} ion doping, *J. Alloys Compd.*, 2019, **777**, 894–901.
44 J. P. C. do Nascimento, A. J. M. Sales, D. G. Sousa, M. A. S. da Silva, S. G. C. Moreira, K. Pavani, M. J. Soares, M. P. F. Graça, J. Suresh Kumar and A. S. B. Sombra, Temperature-, power-, and concentration-dependent two and three photon upconversion in Er^{3+}/Yb^{3+} co-doped lanthanum orthoniobate phosphors, *RSC Adv.*, 2016, **6**(72), 68160–68169.
45 P. Jena, S. K. Gupta, V. Natarajan, O. Padmaraj, N. Satyanarayana and M. Venkateswarlu, On the photoluminescence properties of sol–gel derived undoped and Dy^{3+} ion doped nanocrystalline Scheelite type $AMoO_4$ (A = Ca, Sr and Ba), *Mater. Res. Bull.*, 2015, **64**, 223–232.

